

Hydrodeoxygenation of phenol over Ni/Ce_{1-x}Nb_xO₂ catalystsKaren A. Resende^a, Adriano H. Braga^b, Fabio B. Noronha^{c,d}, Carla E. Hori^{a,*}^a Federal University of Uberlândia, School of Chemical Engineering, Av. João Naves de Ávila, 2121, Bloco 1 K, 38400-098, Uberlândia, Brazil^b University of São Paulo - USP, Institute of Chemistry, Av. Prof. Lineu Prestes 748, São Paulo, Brazil^c National Institute of Technology, Division of Catalysis and Chemical Processes, Av. Venezuela, 82, 20081-312, Rio de Janeiro, Brazil^d Military Institute of Engineering, Chemical Engineering Department, Praça Gal. Tibúrcio 80, 22290-270, Rio de Janeiro, Brazil

ARTICLE INFO

Keywords:

Phenol
Bio-oil
Hydrodeoxygenation
Cerium oxide
Niobium addition

ABSTRACT

This work investigated the effect of different niobium concentration on the performance of Ni/Ce_{1-x}Nb_xO₂ catalyst for hydrodeoxygenation of phenol in gas phase at 300 °C. Also, the structural modification promoted by Nb addition was studied by several techniques. In situ X-ray diffraction and Raman analyses indicated that high niobium concentration lead to Nb₂O₅ oxide with hexagonal structure, while in situ X-ray photoelectron spectroscopy (XPS) experiments indicated an enrichment of the surface with Nb. In general, the incorporation of niobium changed the lattice parameter of ceria and promoted the formation of oxygen vacancies as observed by XPS and X-ray absorption near edge structure (XANES) analyses, which favored the activity of the sample. Increasing Nb content increased the selectivity to deoxygenated products (benzene). The superior benzene selectivity is likely due to the higher interaction between the oxygen of phenol molecule and the oxophilic sites represented by the Nb⁵⁺ cations of the support that promotes the hydrogenation of carbonyl group.

1. Introduction

Usually pyrolytic bio-oil has a high oxygen content, which leads to undesirable properties, such as low energy density, thermal and chemical instability and lower calorific power [1]. The upgrading of bio-oil by hydrodeoxygenation (HDO) is a potential route to the final production of renewable fuels, since this process eliminates oxygen and stabilizes the product [2]. HDO reactions may be performed in gas or liquid phase, however the liquid phase treatments have some disadvantages, such as, the consumption of solvent, the cost of high pressure equipment and the difficulties to separate catalyst, char, products, solvent and non-reacted lignin from the reaction media [3].

The bio-oil obtained from biomass pyrolysis is a complex mixture of reactive and phenolic compounds, which represents the major part of the lignin fraction in this oil [4]. This explains the use of these reagents as model compounds of the bio-oil [5]. In this work, the HDO process was studied in the gas phase using phenol as a model compound.

Several transition metals and their combinations have been studied in HDO reactions [6–9]. According to the literature, bifunctional catalysts containing a combination of an oxophilic support and an active metal phase is the most effective for this process [10]. The metal particles are responsible for hydrogenation/dehydrogenation reactions [11], while the activation of oxy-compounds is promoted by the valence of an oxide support [12].

The support plays an important role in the HDO process, since it can improve the dispersion and stability of the active phase. De Souza et al. [6] investigated the effect of the support (SiO₂, Al₂O₃, TiO₂, ZrO₂, CeO₂ and CeZrO₂) on the performance of Pd-based catalysts for phenol HDO at 500 °C using a fixed bed reactor. Pd/TiO₂ and Pd/ZrO₂ favored the formation of benzene, while cyclohexanone was a major product over the other supports (Pd/SiO₂, Pd/Al₂O₃, Pd/CeO₂ and Pd/CeZrO₂). The high selectivity to benzene over Pd/TiO₂ and Pd/ZrO₂ catalysts was related to the oxophilic sites of these supports represented by low-coordinated Ti⁴⁺/Ti³⁺ and Zr⁴⁺/Zr³⁺ cations near the periphery of metal particles. Although Pd/CeO₂ and Pd/CeZrO₂ catalysts were poorly selective to deoxygenated products, these samples showed the best stability for phenol HDO.

Over the past several years, CeO₂-containing materials have been intensively studied as catalysts of heterogeneous reactions. The presence of ceria in the catalyst is justified by the possible improvement in the reaction activity and selectivity caused by the presence of the redox couple Ce⁴⁺-Ce³⁺. Schimming et al. [13] investigated the hydrodeoxygenation of guaiacol over bulk ceria and ceria-zirconia oxides with different elemental compositions. Ceria-zirconia catalysts without fully reduced metal particles are active for the studied reaction, benzene was formed as the completely deoxygenated product, but the final deoxygenation step is much slower than the hydrogenation. According to the authors Ce-oxide dissociates hydrogen and creates oxygen vacancy sites under mild conditions, which is a requirement for HDO

* Corresponding author.

E-mail address: cehori@ufu.br (C.E. Hori).<https://doi.org/10.1016/j.apcatb.2018.12.040>

Received 3 August 2018; Received in revised form 3 December 2018; Accepted 15 December 2018

Available online 17 December 2018

0926-3373/ © 2018 Elsevier B.V. All rights reserved.

catalysts. The presence of zirconium causes a slight strain in the ceria–zirconia crystal lattice and facilitates structural relaxation after the formation of oxygen vacancies.

Several cerium mixed oxides Ce–M–O (with M = Eu, Pr, Sm, Nd) were recently investigated with the aim of improving oxygen mobility on this oxide [14]. The distortion of sub lattices of ceria caused by the presence of another element allows a higher mobility of lattice oxygen. Thus, besides zirconium [15–17], another promoting metal could be added to the cerium oxide structure aiming to improve the performance for HDO reactions, although so far there are no successful reports in the literature. Niobium is a potential metal to be added to ceria, given that this transition metal strongly favors the deoxygenation of phenolic compounds over HDO reaction conditions [8], as shown in previous studies [18–29]. In general, interactions among different components of mixed oxides strongly affect their structure and catalytic performance.

Therefore, this work aims to investigate the effects of Nb addition to ceria structure and the effects on activity and selectivity over gas phase hydrogenation of phenol, using nickel as a metallic phase. The structural modification promoted by Nb addition in different environments was studied by in situ X-ray photoelectron spectroscopy (XPS), and in situ X-ray absorption spectroscopy (XAS) and X-ray diffraction (XRD) experiments.

2. Experimental

2.1. Catalyst preparation

Cerium oxide and niobium doped cerium oxide were synthesized by precipitation or co-precipitation method [21]. An aqueous solution of cerium (IV) ammonium nitrate (ACS 98.5%) and niobium oxalate (CBMM) was prepared in order to obtain the desired amounts of $\text{Ce}_x\text{Nb}_{1-x}\text{O}_2$ ($x = 0.80$ and 0.30). A precipitate was formed by the addition of an excess of ammonium hydroxide. Finally, the precipitate was washed with distilled water and calcined at 600°C for 2 h. For the preparation of Nb_2O_5 , niobic acid (CBMM) was calcined in air flow at 350°C for 2 h. Nickel supported samples were prepared by incipient wetness impregnation of the supports with an aqueous solution of $(\text{NO}_3)_2.6\text{H}_2\text{O}$ (Vetec 97%). After impregnation, the material was dried at 100°C for 12 h and then calcined in air at 350°C for 6 h ($10^\circ\text{C min}^{-1}$). All the samples contained 10 wt.% of Ni. The catalysts were designated as Ni/CeO₂, Ni/Ce_{0.80}Nb_{0.20}O₂, Ni/Ce_{0.30}Nb_{0.70}O₂ and Ni/Nb₂O₅, which followed the nominal composition desired.

2.2. Catalyst characterization

The chemical composition of the samples was determined using a Wavelength Dispersive X-Ray Fluorescence Spectrometer (WD-XRF) S8 Tiger, Bruker with a rhodium tube operated at 4 kW. The analyses were performed with the samples (300 mg) in powder form using a semi-quantitative method (QUANT-EXPRES/Bruker). BET surface areas of the samples were measured using a Micromeritics ASAP 2020 analyzer by nitrogen adsorption at -196°C . Raman spectroscopy was used to characterize the structure of the calcined samples. The Raman spectra were recorded using a LabRam HR-UV800/JobinYvon, equipped with CCD detector (cooled at -120°C with liquid N₂) and excitation source of 632 nm. Temperature programmed reduction (TPR) was performed in a quartz reactor coupled to a mass spectrometer (Hidden Analytical, QGA). Prior to a TPR experiment, the sample was pretreated at 100°C under inert atmosphere. The reducing mixture (1.96% H₂ in Ar) was passed through the sample (100 mg) and the temperature was increased from room temperature to 1000°C at a heating rate of $10^\circ\text{C min}^{-1}$.

In situ X-ray diffraction (XRD) analyses were obtained at XPD beam-line at the Brazilian Synchrotron Light Laboratory (LNLS), Campinas-SP, Brazil. A wavelength of 1.5498 \AA at 8.17 keV was used. Powder samples were placed in a round furnace with Kapton windows, allowing heating, gas stream feeding and recording of XRD data. XRD patterns were

obtained by a Mythen – 1 K detector (Dectris) installed 1 m from the furnace. The calcined catalysts were submitted to reduction under flow of 5% H₂ in He (100 mL min^{-1}) from room temperature to 500°C ($10^\circ\text{C min}^{-1}$), and kept at this temperature for 1 h, with XRD data acquisition.

X-ray photoelectron spectroscopy (XPS) analyses of the samples were performed at LNLS with a hemispherical spectrometer from SPECS (model PHOIBOS150 HSA3500) using a monochromatic Al K_α X-ray (1486.7 eV) source for excitation and a spherical section analyzer. The monochromatic Al K_α source was operated at 10 kV and 10 mA and the spectra were obtained with an analyzer pass energy of 20 eV. The spectra were analyzed using Casa XPS software, version 2.2.99. The binding energies were referenced to the C 1s line at 284.5 eV from the adventitious carbon. The analyses were performed before and after the reduction of the samples. The reduction treatment consisted of heating the samples under a 5% H₂/Ar mixture from room temperature to 500°C , holding at this temperature for 1 h in a pre-chamber. Then, the sample was cooled to room temperature under 5% H₂/Ar mixture, outgassed to 10^{-8} mbar and transferred to the main spectrometer chamber under vacuum without any exposure to air.

In situ X-ray absorption near edge spectroscopy (XANES) measurements at the Ce L_{III}-edge (5723 eV) were performed at the DXAS beam-line at the LNLS. DXAS is a dispersive beamline equipped with a curved Si (111) focusing monochromator operating in Bragg mode and the X-ray range varies from 4 to 14 keV focusing the beam at the sample position. The detection system is comprised of 1152×1242 (500×900) pixel CCD solid-state detector. The samples were placed in a quartz reactor and reduced under diluted hydrogen (5% H₂ balance in He) with a total flow of 100 mL min^{-1} and a heating rate of the $10^\circ\text{C min}^{-1}$ from room temperature to 500°C (1 h). Athena software packages were used to extract the XANES signal from the measured absorption spectra using standard proceedings. XANES spectra of reference materials (CeO₂ and cerium nitrate) were also recorded at room temperature.

X-ray absorption spectra (XAS) were acquired in transmission mode at the Nb K-edge (18986 eV) and Ni K-edge (8333 eV) using the XDS and XAFS-2 beamlines at LNLS, Campinas-SP, Brazil. Two monochromators were used as follows: a Si(311) crystal for the Nb-K edge and a Si(111) crystal for the Ni-K edge. Intensities were measured using three sequential ionization chambers filled with mixtures of N₂ and Ar at ambient temperature and 1 bar of pressure. Photon energies were calibrated using a thin metal foil (Ni or Nb) placed between the second and third ionization chambers. Spectra were collected at the absorption edge for each metal present in a range between 200 eV before and 120 eV after for Nb K-edge and 200 eV before and 1000 eV after for Ni K-edge. The samples were also reduced under a 5% H₂/Ar mixture from room temperature to 500°C , holding at this temperature for 1 h. After reduction, the samples were cooled to ambient temperature under Helium flow (100 mL min^{-1}) and the spectra were recorded. Data reduction of the EXAFS/XANES spectra was carried out using the Artemis program. EXAFS data treatment was performed using the WinXAS (Ressler14), Atoms (Ravel16), FEFF (Rehr17), and FEFFIT (Ravel18) softwares. The k-range used for the fittings was $2.75\text{--}14.16\text{ \AA}^{-1}$. Fitting was confined to the first Ni-Ni coordination shell by applying a Hanning window in the Fourier transform magnitude spectra, and carrying out the back-transform to isolate that shell.

Transmission electron microscopy (TEM) images were acquired in a Jeol 2010 F microscope, with a field emission gun operating with 200 kV of acceleration voltage. The reduced catalysts were grounded and dispersed in methanol with sonication and dropped in a hollow carbon coated Cu grid. High resolution images were acquired in a GatanTridien CCD detector. EDS spectra and chemical mapping were obtained in STEM mode, with a silicon-drift detector X-MaxN 100TLE from Oxford Instruments.

2.3. Activity tests

HDO of phenol was carried out in a fixed-bed quartz reactor,

operating at atmospheric pressure of H_2 and 300 °C. Prior to reaction, the sample was reduced in situ under pure hydrogen (60 mL min^{-1}) at 500 °C for 1 h. The catalysts were diluted with inert material ($m_{SiC}/m_{catal} = 3.0$) to avoid the formation of hot-spots. The reactant mixture (1.6% of phenol) was obtained by flowing H_2 through the saturator containing phenol, which was kept at the specific temperature ($\sim 70^\circ\text{C}$) required to obtain a H_2 /phenol molar ratio of 60. To avoid condensation, all gas stream lines were heated at 250 °C. The reaction products were analyzed using an Agilent Technologies 7890 A/5975C GCMS, equipped with an HP-Innowax capillary column and a flame-ionization detector (FID). The catalysts were evaluated at different residence time (W/F) by varying the catalyst amount in the range of 2.5–200 mg. The W/F is defined as the ratio of catalyst mass (g) to organic feed mass flow rate (g/h). The stability tests were performed during 24 h of time on stream (TOS), using W/F value corresponding to the highest phenol conversion obtained. The product yield and selectivity for each product were calculated as follows (Eqs. (1) and (2)):

$$\text{yield}(\%) = \frac{\text{mol of product produced}}{\text{mol of phenol fed}} \times 100 \quad (1)$$

$$\text{selectivity}(\%) = \frac{\text{mol of product produced}}{\text{mol of phenol consumed}} \times 100 \quad (2)$$

The stability of the catalysts was defined as the ratio between the reaction rate at $t_0 = 0.2\text{ h}$ and $t_f = 24\text{ h}$ TOS, assuming first-order kinetics. Therefore, a deactivation parameter (DP) can be given by Eq. (3).

$$DP = \frac{\ln(1 - X_{\text{end}})}{\ln(1 - X_{\text{initial}})} \quad (3)$$

3. Results and discussion

3.1. Catalyst characterization

Table 1 shows the surface area and the metal loadings of the calcined samples. The samples have almost similar specific surface areas. As the Nb concentration increased, BET surface area decreased, which was also observed by Stošić et al. [22]. Ni content values were close to the nominal one (10 wt.%) for all samples. Also, Ce/Nb molar ratios measured were close to the expected ones.

Raman spectroscopy was used to investigate the effect of Nb addition on the structure of the $Ce_xNb_{1-x}O_2$ supports. Raman spectra of the oxides are shown in Fig. S1 (supplementary material). The Raman spectra of the Nb_2O_5 presented a band around 690 cm^{-1} due to NbO_6 octahedra species [30,31]. According to Pittman and Bell [32], the presence of the orthorhombic (T) or hexagonal (TT) Nb_2O_5 crystal phases gives rise to the Raman band at 692 cm^{-1} . T- Nb_2O_5 is composed with highly distorted octahedral and pentagonal bipyramidal Nb environments rather than regular octahedral [31]. The TT-phase is a metastable structure similar to those of T- Nb_2O_5 , which details are not fully understood [31]. The distinction between the two phases is difficult on the basis of Raman spectroscopy alone. The broad peaks located between 200 and 400 cm^{-1} can be attributed to the bending vibrations of Nb-O-Nb bond [30]. For CeO_2 , the Raman spectrum exhibited a band at 464 cm^{-1} , which is attributed to the symmetric stretching of Ce-O bonds

Table 1
Surface area and chemical composition determined by XRF of the calcined samples.

Samples	BET area ($\text{m}^2\text{ g}^{-1}$)	Ni(%)	CeO ₂ (%)	Nb ₂ O ₅ (%)	Ce/Nb
Ni/CeO ₂	20	–	–	–	–
Ni/Ce _{0.80} Nb _{0.20} O ₂	28	9.1	61.3	26.7	5.0
Ni/Ce _{0.30} Nb _{0.70} O ₂	15	10.2	14.5	72.5	0.4
Ni/Nb ₂ O ₅	7	–	–	–	–

for a metal oxide with cubic fluorite structure [33,34]. The Raman spectra of $Ce_{0.80}Nb_{0.20}O_2$ is similar to that of CeO_2 , however a small shift of this Raman band to lower frequencies (460 cm^{-1}) was observed for $Ce_{0.80}Nb_{0.20}O_2$. Vidal et al. [35] observed that the incorporation of Zr or Pr into the fluorite structure of CeO_2 induced a shift of the main band to lower frequency, around 460 cm^{-1} . Increasing the Nb content changed completely the Raman spectrum. In fact, the spectrum of $Ce_{0.30}Nb_{0.70}O_2$ sample is similar to that of Nb_2O_5 , showing also a band around 690 cm^{-1} , which could be an indication of orthorhombic or hexagonal Nb_2O_5 crystal phases in this sample. Therefore, the $Ce_xNb_{1-x}O_2$ samples with x between 1.00 and 0.80 have a cubic structure whereas the sample with $x \leq 0.30$ exhibits an orthorhombic or hexagonal structure.

TEM images of the calcined $Ce_{0.80}Nb_{0.20}O_2$ and $Ce_{0.30}Nb_{0.70}O_2$ with the chemical composition of selected areas measured by EDS are shown in Fig. 1. The chemical mapping of the $Ce_{0.80}Nb_{0.20}O_2$ sample shows that Nb and Ce are not homogeneously distributed. For $Ce_{0.30}Nb_{0.70}O_2$, the EDS results indicated that Nb and Ce have analogous distributions in the particle. This different behavior of the Nb and Ce distribution for both samples can be related to structure.

Fig. 2 shows the diffractograms of calcined Ni-supported catalysts. All the samples exhibited the characteristic lines of NiO at $2\theta = 37.31$ and 43.37° . For Ni/CeO₂ and Ni/Ce_{0.80}Nb_{0.20}O₂, the lines corresponding to CeO₂ (ICSD-72155) with cubic structure ($2\theta = 28.69^\circ$, 32.75° , 47.73° and 55.21°) were also observed [36]. This result agrees very well with the Raman spectra of the supports. The peaks related to Nb_2O_5 were not detected, which may be an indication that Nb was incorporated into ceria's lattice or niobium oxide is highly dispersed on CeO₂ or amorphous [15,28,37–39].

For Ni/Ce_{0.30}Nb_{0.70}O₂ and Ni/Nb₂O₅ catalysts, the lines corresponding to CeO₂ were no longer detected, and only peaks typical of Nb_2O_5 and nickel oxide were observed. Ni/Ce_{0.30}Nb_{0.70}O₂ showed the lines characteristic of Nb_2O_5 with pseudohexagonal structure [40–42], while the diffractogram of Ni/Nb₂O₅ corresponds to an orthorhombic Nb_2O_5 structure (JCPDS 27-1003). The pseudohexagonal form has structure similar to that of orthorhombic Nb_2O_5 phase, however it is less crystallized [41]. In general, the diffraction data of pseudohexagonal Nb_2O_5 has been described as a disordered modification of orthorhombic Nb_2O_5 [31].

In order to obtain the lattice parameters of the supports, the UNITCELL software package was used. UNITCELL is a least squares refinement program to retrieve unit cell constants from diffraction data and the program is further described by Holland and Redfern [43]. As the diffractograms of Ni/Ce_{0.80}Nb_{0.20}O₂ showed the phases corresponding to CeO₂, the cubic structure was used in the calculations. For Ni/Ce_{0.30}Nb_{0.70}O₂, the hexagonal structure was considered, since the main peaks observed in the diffractograms were related to Nb_2O_5 with pseudohexagonal structure, while for Ni/Nb₂O₅, the orthorhombic structure was used.

The lattice parameter calculated for Ni/CeO₂ sample was equals to 5.3845 \AA (Table 2), which agrees well with the lattice parameter reported for Ni/CeO₂ in the literature [42,44]. For Ni/Ce_{0.80}Nb_{0.20}O₂ samples, the addition of Nb decreased the lattice parameter (5.3740 \AA). In the case of the formation of a solid solution between CeO₂ and niobium oxide, the Nb^{5+} atoms (0.7 \AA) would occupy the position of the larger Ce^{4+} atoms (0.96 \AA), which favors the decrease of cell volume. Doping CeO₂ lattice with Nb will induce a uniform strain in the lattice as the material is elastically deformed [45]. Similar results are reported in the literature for CeZrO₂ materials [44], where the substitution of Ce^{4+} cations by a smaller Zr^{4+} cation (0.84 \AA) in the lattice leads to a decrease in the lattice parameter and a shift of the ceria lines towards higher angles. Regarding Ce-Nb mixed oxides, although Ramírez-Cabrera et al. [45] estimated that 1.4% Nb would be the solubility limit of Nb in CeO₂, they pointed out that the incorporation of a higher amounts of Nb could be possible. Therefore, in this work it is expected that just a part of the niobium added to the sample was

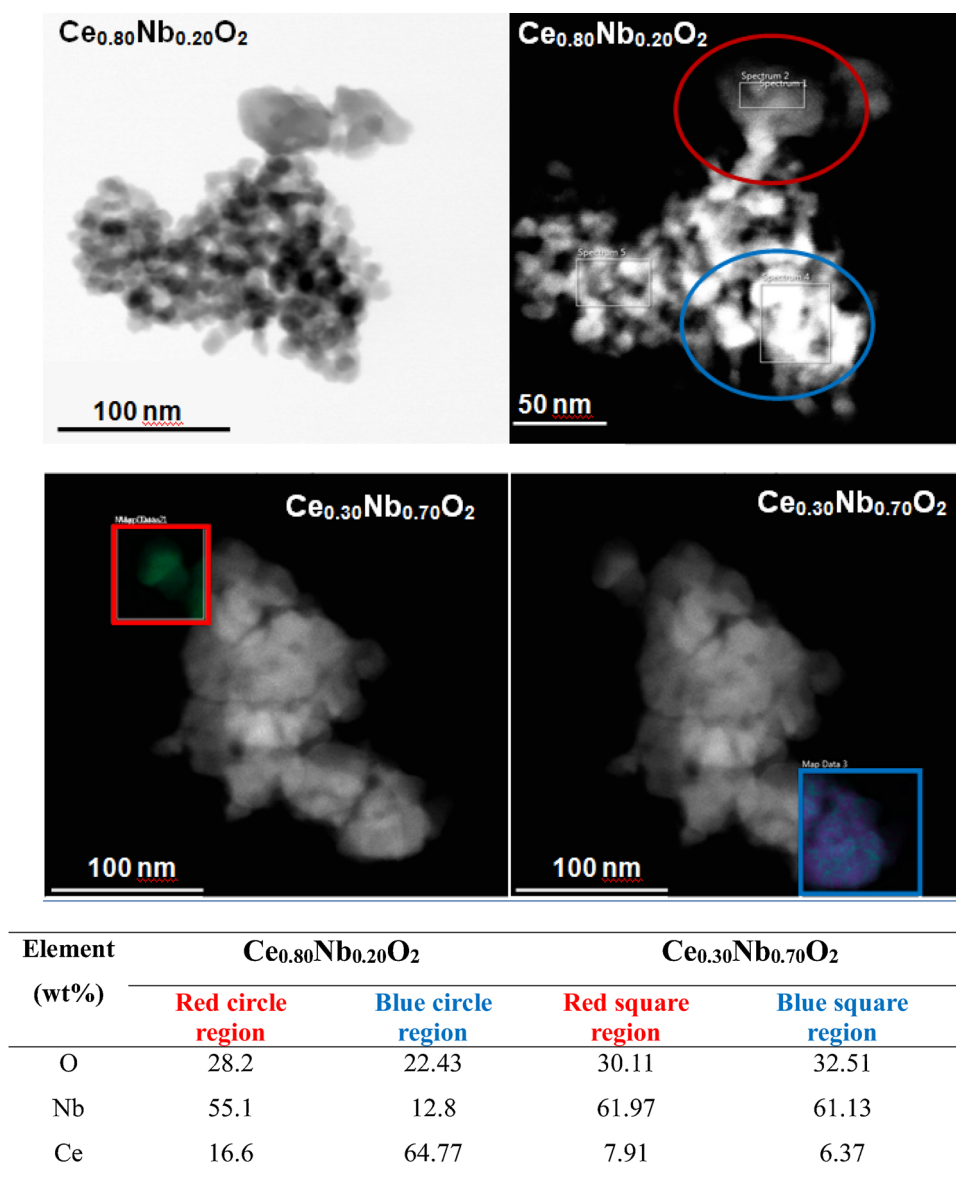


Fig. 1. TEM image and EDS of selected areas of Ce_{0.80}Nb_{0.20}O₂ and Ce_{0.30}Nb_{0.70}O₂.

incorporated to the cerium oxide structure. For Ni/Ce_{0.30}Nb_{0.70}O₂ and Ni/Nb₂O₅ the values of the crystallographic parameters observed are similar to the ones previously reported [40].

In situ XRD measurements were conducted under a mixture of 5% H₂ in He and collected at 298–500 °C temperature range. The diffractograms of Ni-supported catalysts are presented in Fig. S2 (supplementary material). For Ni/CeO₂ catalyst, the lines corresponding to the cubic fluorite phase of CeO₂ (ICSD-72155) and NiO (ICSD-9866) can be clearly seen between 25 and 100 °C. At 200 °C, the lines related to Ni⁰ (2θ = 44.5° and 52°) start to appear, indicating that the reduction of nickel oxide started. Similar behavior was observed for Ni/Ce_{0.80}Nb_{0.20}O₂. For this sample the lines characteristic of CeO₂ were shifted to smaller 2θ values as the temperature was increased, which is likely due to cerium oxide reduction [44]. The diffractograms for Ni/Ce_{0.30}Nb_{0.70}O₂ and Ni/Nb₂O₅ exhibited the lines attributed to pseudo-hexagonal and orthorhombic Nb₂O₅ phases, respectively, in the whole temperature range. However, the lines characteristic of Nb₂O₅ remained unchanged with the increase of temperature. For these samples, the lines characteristic of NiO phase were also detected up to 200 °C. Increasing the temperature to 300 °C led to a complete reduction of NiO and the appearance of the lines typical of metallic Ni.

The CeO₂ lattice parameter was calculated for Ni/CeO₂ and Ni/Ce_{0.80}Nb_{0.20}O₂ as a function of temperature during the reduction process and the results were plotted in Fig. 3. In general, the CeO₂ lattice parameter increased with the temperature in H₂ atmosphere. For Ni/CeO₂, a linear increase in the lattice parameter was observed between 200 and 500 °C, while a non-linear relationship was obtained for Ni/Ce_{0.80}Nb_{0.20}O₂ at the same temperature range. The linear increase in the lattice parameter can be ascribed mainly to the thermal expansion effect [46,47]. However, the non-linear increase of the lattice parameter can be mainly an indication of the reduction of ceria. According to Rossignol et al. [46], the reduction of Ce⁴⁺ to Ce³⁺ cations leads to a ceria lattice expansion because the Ce³⁺ is larger than Ce⁴⁺. Therefore, the non-linear relationship between the lattice parameter and reduction temperature observed for Ni/Ce_{0.80}Nb_{0.20}O₂ under H₂ atmosphere could be attributed to two phenomena [46]: (i) the intrinsic thermal expansion of sample holder and (ii) lattice expansion due to the reduction of Ce⁴⁺ to Ce³⁺.

Table 3 lists the average crystallite size of cerium oxide, NiO and metallic nickel estimated by the Scherrer equation. For Ni/CeO₂, the crystallite size of CeO₂ was 21 nm and it did not change with the increase of the reduction temperature. The addition of Nb to ceria

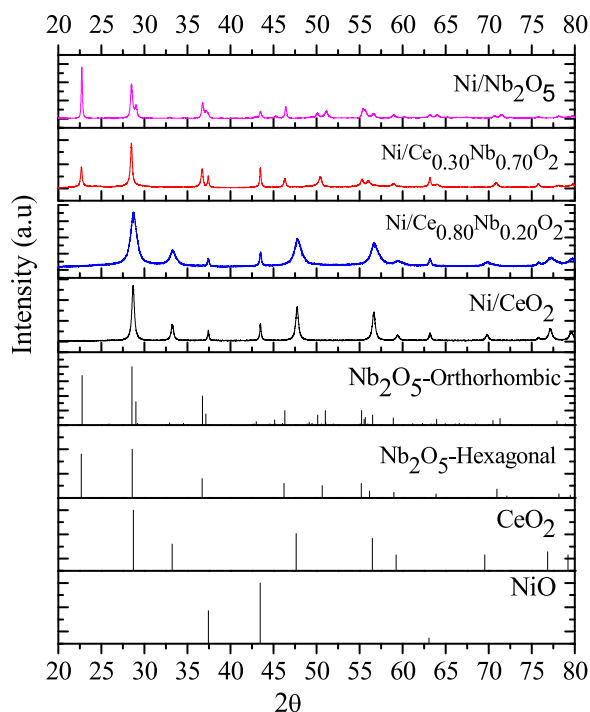


Fig. 2. Diffractogram of Ni-supported calcined samples.

significantly decreased the crystallite size of CeO_2 , which is an indication that the addition of Nb increased the sintering resistance of the cerium oxide. $\text{Ni/Ce}_{0.80}\text{Nb}_{0.20}\text{O}_2$ exhibited average CeO_2 crystallite size around 8–10 nm, regardless of the reduction temperature.

NiO average crystallite size at room temperature varied from 30 nm ($\text{Ni/Ce}_{0.80}\text{Nb}_{0.20}\text{O}_2$) to 38 nm (Ni/CeO_2 and $\text{Ni/Ce}_{0.30}\text{Nb}_{0.70}\text{O}_2$) (Table 3). At 300 °C, NiO was completely reduced and the values reported in Table 3 correspond to the average crystallite size of metallic Ni [48]. For Ni/CeO_2 , the crystallite size of metallic nickel was around 33 nm at 300 °C and increased significantly (2-fold) when the reduction temperature increased to 500 °C. Similar behavior was observed for $\text{Ni/Ce}_{0.30}\text{Nb}_{0.70}\text{O}_2$, $\text{Ni/Nb}_2\text{O}_5$, and $\text{Ni/Ce}_{0.80}\text{Nb}_{0.20}\text{O}_2$.

Aiming to evaluate the oxidation states of niobium after the reduction at different temperatures, TPR-XANES analysis was performed. XANES spectra of the samples after reduction at 500 °C (Fig. 4A) show a pre-edge absorption and two peaks in the post-edge region. The pre-edge absorption feature was observed around 18,996 eV, which is related to an electronic transition from the Nb 1s orbital to the 5p orbital [49–52]. The two features located at around 19,005 and 19,017 eV reflect the low-energy scattering resonances of photoelectrons by neighboring atoms [53]. The intensity of the peak around 19,005 eV decreases when the Ce content increases.

Fig. 4B presents a comparison of the first derivative of XANES spectra at the Nb K-edge for all the samples after the reduction at 500 °C for 1 h. According to the literature [53,54] XANES spectra of niobium

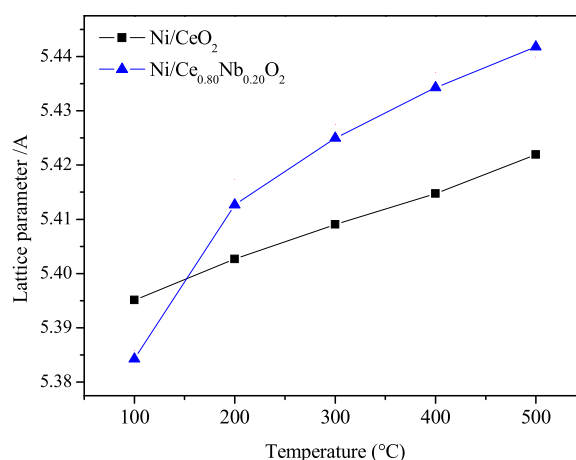


Fig. 3. Variation of the lattice parameter with temperature under H_2 atmosphere.

oxides are somewhat similar, although the first derivative of these spectra can show distinct features relative to different niobium oxides. In general, the presence of cerium oxide slightly affects the Nb K edge XANES spectra profiles of the studied samples and the highest difference is observed between $\text{Ni/Nb}_2\text{O}_5$ and $\text{Ni/Ce}_{0.80}\text{Nb}_{0.20}\text{O}_2$ (Fig. 4B). The white line intensity of the reference samples is also affected by Nb oxidation state, as well as the shape of the spectra [50]. For $\text{Ni/Ce}_{0.80}\text{Nb}_{0.20}\text{O}_2$ a small peak around 18,986 eV is observed. These results could be an indication that the addition of Ce to niobia promoted the reduction of some Nb^{5+} species in this sample [54].

Fig. 5 shows the in situ XANES spectra at Ce L_{III} -edge during reduction. Comparisons between the spectra of calcined samples and after reduction at 500 °C are shown in Fig. 6. At room temperature, all samples showed two peaks (5728.3 and 5735.3 eV) [55], which are related to Ce^{4+} species (Fig. 6a). These peaks correspond to absorption into the 5d level with no occupancy in the 4f level in either the initial or final state [56]. When the temperature was increased, there were no significant changes on the spectra of Ni/CeO_2 catalyst. However, the spectra strongly changed for the Nb-doped samples during reduction. The intensity of the shoulder at around 5727 eV significantly increased as the reduction temperature increased. This shoulder is characteristic of Ce^{3+} species, indicating that the addition of Nb favored the conversion Ce^{4+} to Ce^{3+} species during the reduction (Fig. 6b). This change was more significant for the sample with higher Nb content.

The evolution of the fraction of Ce^{4+} and Ce^{3+} species as a function of reduction temperature is better seen by the curves of linear combination fittings (Fig. S3). Table S1 shows the Ce^{3+} fraction values observed after reduction at 500 °C. CeO_2 and $\text{Ce}(\text{NO}_3)_3$ spectra were used as references for the linear combination fittings. For Ni/CeO_2 catalyst, the reduction of Ce^{4+} to Ce^{3+} species started around 250 °C (Fig. S3). The beginning of ceria reduction started at lower temperature for $\text{Ni/Ce}_{0.80}\text{Nb}_{0.20}\text{O}_2$ catalyst (200 °C). Furthermore, a higher fraction of Ce^{3+} species was obtained in this catalyst (0.53) after reduction at 500 °C in comparison to Ni/CeO_2

Table 2
Refined crystallographic parameters analysis of synchrotron X-ray powder diffraction data.

Sample	Structure	a	b	c	Cell Volume (Å ³)
Ni/CeO_2	Cubic	5.3845 (± 0.00024)	–	–	156.1130 (± 0.0209)
$\text{Ni/Ce}_{0.80}\text{Nb}_{0.20}\text{O}_2$	Cubic	5.3761 (± 0.00024)	–	–	155.3846 (± 0.0207)
$\text{Ni/Ce}_{0.30}\text{Nb}_{0.70}\text{O}_2$	Hexagonal	3.6168 (± 0.00028)	–	3.9174 (± 0.00035)	44.3804 (± 0.0075)
$\text{Ni/Nb}_2\text{O}_5$	Orthorhombic	6.1191 (± 0.00076)	29.1083 (± 0.00661)	3.9090 (± 0.00036)	696.2692 (± 0.1521)

Table 3
Average crystallite sizes estimation based on Scherrer Equation.

Temp (°C)	NiO/Ni ^o (nm)			
	Ni/CeO ₂	Ni/Ce _{0.80} Nb _{0.20} O ₂	Ni/Ce _{0.30} Nb _{0.70} O ₂	Ni/Nb ₂ O ₅
RT ^a	38	30	38	31
300	33	29	37	36
400	46	33	45	33
500	57	44	53	51
500-1 h	60	47	61	57

Temp (°C)	CeO ₂ (nm)			
	Ni/CeO ₂	Ni/Ce _{0.80} Nb _{0.20} O ₂	Ni/Ce _{0.30} Nb _{0.70} O ₂	Ni/Nb ₂ O ₅
R.T	21	9	10	–
500-1 h	22	9	8	–

^a NiO nickel oxide average crystallite size.

(0.15). With the increase of the Nb content, the reduction of CeO₂ started at lower temperature. Furthermore, the addition of Nb also increased the extent of CeO₂ reduction. A similar result has been reported for CeZrO₂ materials [57]. In the case of Zr, it is well known that the introduction of Zr atoms to ceria lattice creates more defects and increases the oxygen mobility in the structure, facilitating the reduction process. The results of our work demonstrate that Nb atoms were inserted in the ceria lattice, resulting in the promotion of Ce⁴⁺ to Ce³⁺ reduction.

In situ XANES spectra at Ni K-edge during reduction of the catalysts are shown in Fig. 7. Ni-K edge XANES spectra for the calcined samples show the presence of NiO [58]. The intensity of the white line decreased as the reduction temperature increased up to 500 °C, which suggests the progressive reduction of NiO to metallic Ni. There were no significant changes on XANES spectra during reduction at 500 °C for 1 h.

The corresponding linear combination fittings of these spectra are presented in Figure S4. The initial spectra of the calcined samples and the Ni foil were used as references for the linear combination fittings. The reduction of NiO to Ni^o starts at 280 °C for Ni/CeO₂ and similar result was observed for all samples, as observed in XRD analysis. At 500 °C, complete reduction of NiO was observed for all catalysts. Therefore, the presence of Nb did not lead to the formation of a nickel phase with low reducibility. In general, the cerium oxide reduction started along with that of NiO (Figures S3 and S4). Once the metallic Ni is formed, the spillover of the hydrogen favors the reduction of ceria [58].

EXAFS spectra of the calcined sample and after reduction at 500 °C are provided in Figure S5. The spectra of calcined samples are

dominated by the Ni-O bond. For all samples, the EXAFS spectra following reduction at 500 °C exhibits one peak located between 2 and 2.5 angstroms in the phase-uncorrected Fourier transform magnitude spectra, which can be assigned to the first Ni-Ni coordination shell. XRD in situ data also indicated the presence of metallic Ni after reduction at 500 °C for 1 h.

The raw k²-weighted $\chi(k)$ spectra filtered (solid black line) and fitted k²-weighted $\chi(k)$ spectra (red filled circles) of the reduced catalysts are shown in Figure S6. According to these data, there are not differences in the spectra of Ni/Ce_xNb_{1-x}O₂ catalysts compared with Ni/CeO₂ and Ni/Nb₂O₅. Therefore, metallic Ni is present on all samples and a NiNb phase was not detected.

EXAFS fitting parameters of all catalysts, as well as for the Ni foil reference are given in Table 4. The goodness of fit parameter were less than 0.009, indicating good fits. The coordination number of the first Ni-Ni shell for all the samples determined by curve-fitting was around 12, which indicates the presence of large metallic Ni particles, which is in agreement with XRD results. All samples exhibited similar Ni-Ni distance, around 2.48 Å. The Debye-Waller factors for the reduced catalysts are slightly higher than for Ni foil, which can be related with a slightly more disordered structure.

XPS technique provided information about the oxidation states for all elements on the surface as well as their surface concentration. The XP spectra of Ni2p_{3/2}, Nb3d, and Ce3d core electron levels for the calcined samples and after reduction at 500 °C are shown in Fig. 8. By performing a peak fitting decomposition, the Ni 2p_{3/2} spectra for all the

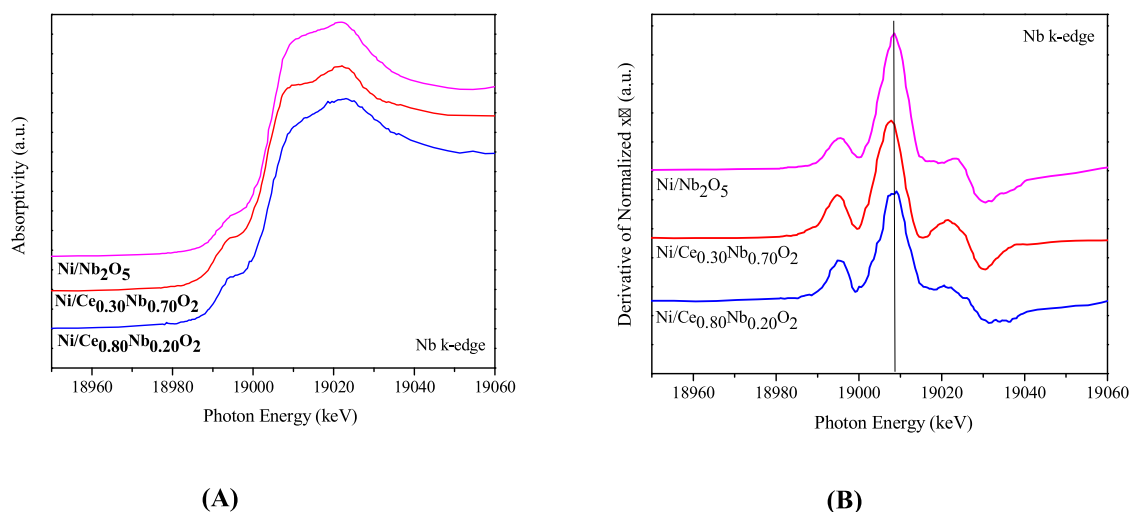


Fig. 4. (A) Comparison of the normalized Nb K-edge XANES spectra of the catalysts after reduction at 500 °C for 1 h; (B) First derivative of Nb K-edge XANES spectra from (A).

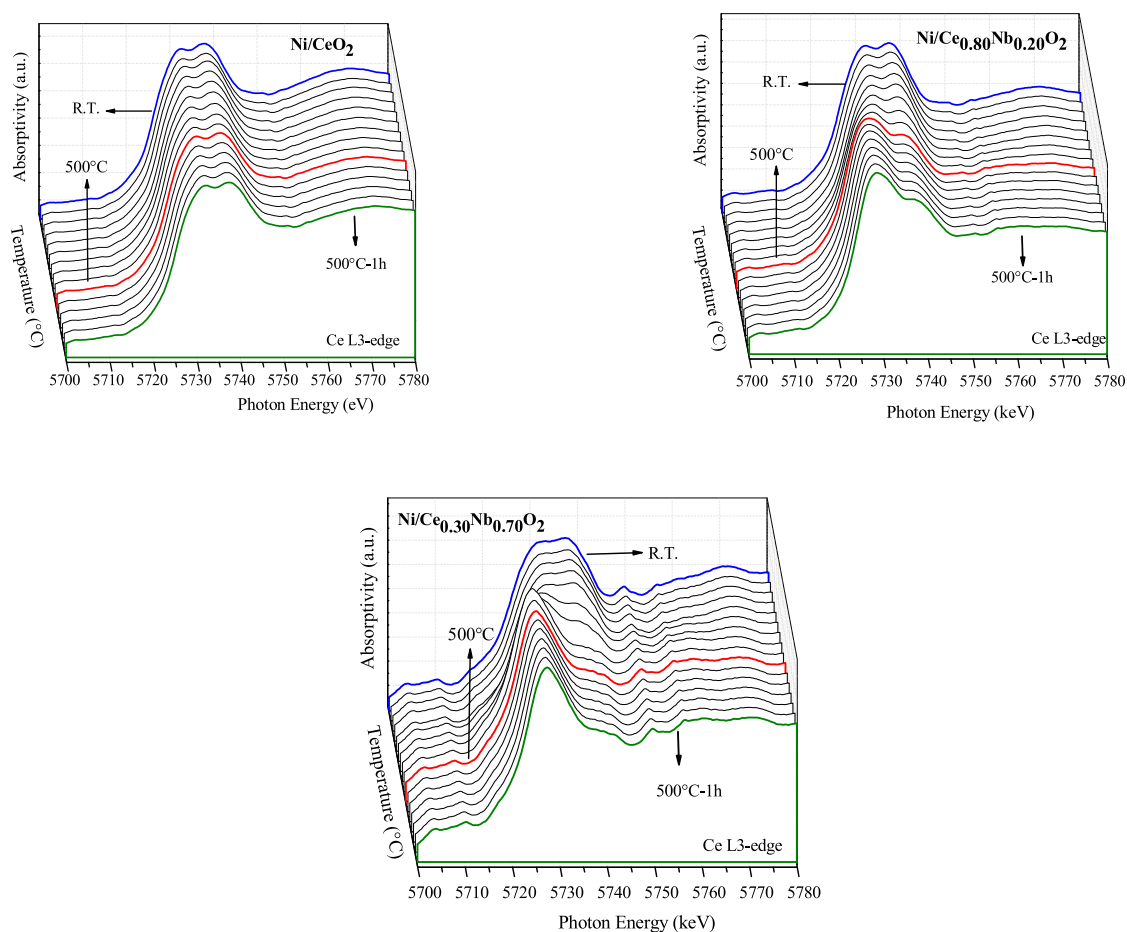


Fig. 5. XANES spectra at Ce L_{III}-edge during reduction of Ni/Ce_xNb_{1-x}O₂ samples under 5% H₂/He mixture.

calcined samples show the main peak with two clearly visible components at 853.5 and 855.3 eV. The former can be ascribed to the surface Ni²⁺ species with octahedral coordination (O_h), and the latter could be attributed to the surface Ni³⁺ species. The satellite peak signal is also observed at 860.7 eV [59,60]. Table 5 lists the surface composition derived from the XPS analyses.

The spectra of the Nb3d region varied significantly depending on the Nb content. For calcined Ni/Ce_{0.30}Nb_{0.70}O₂ and Ni/Ce_{0.80}Nb_{0.20}O₂

two peaks with the binding energy value around 207.2 eV and 209.4 eV were observed, which is related to Nb₂O₅ [22,25,26,49]. For Ni/Ce_{0.80}Nb_{0.20}O₂, there is an additional peak (blue curve) at low B.E. that can be assigned to Nb⁴⁺ species. According to You et al. [19], Nb⁴⁺ and Ce⁴⁺ species are formed by the redox reaction between Ce³⁺ (defect site) and Nb⁵⁺ on NbO_x/CeO₂ catalysts. The authors showed that the Nb⁵⁺ precursor preferentially interacts with surface oxygen vacancies on CeO₂ rods, resulting in decreased surface oxygen vacancy

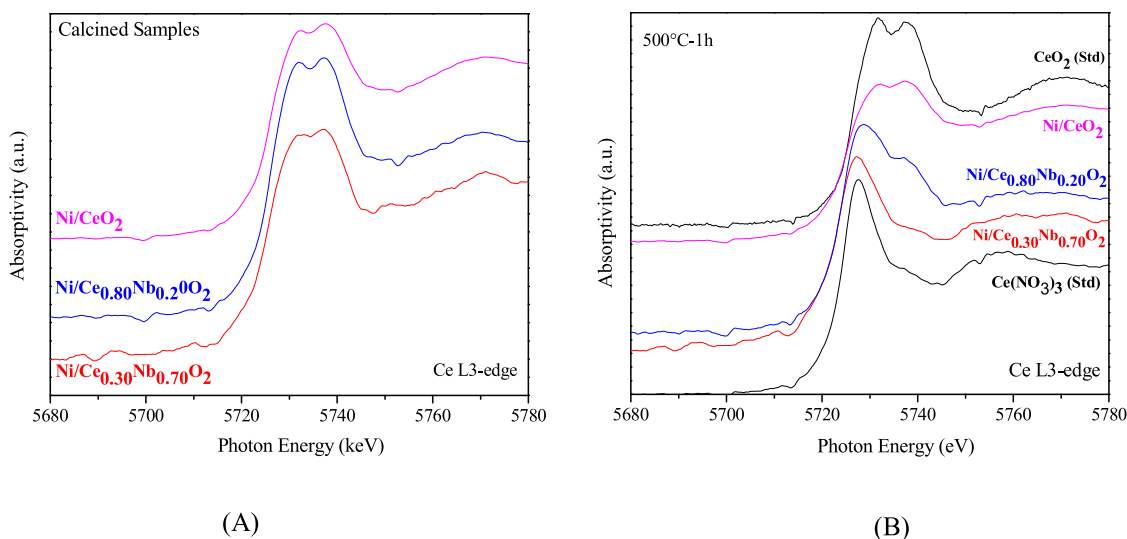


Fig. 6. Comparison of the normalized Ce L_{III}-edge XANES spectra of calcined samples and after the reduction at 500 °C.

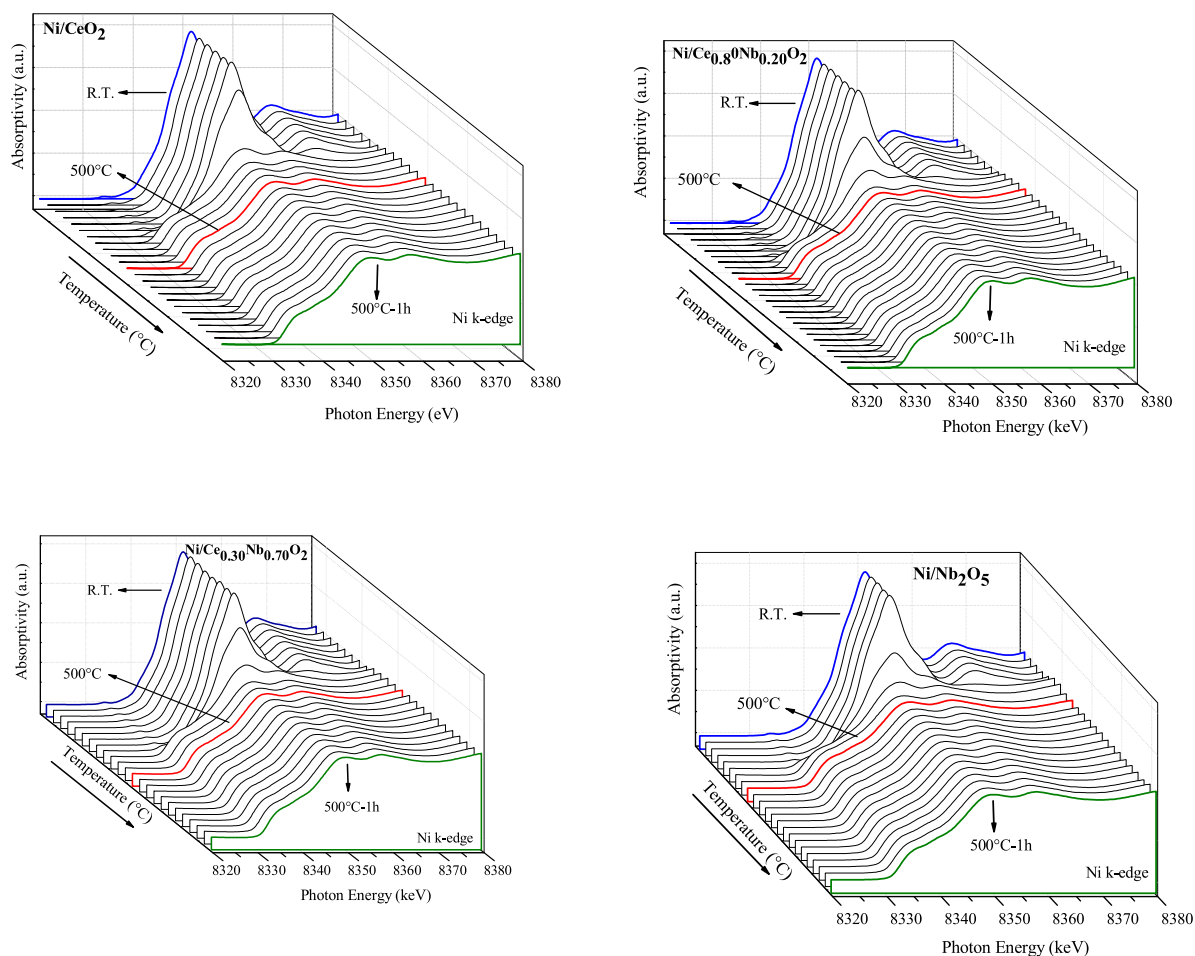


Fig. 7. XANES spectra at the Ni K-edge during reduction of $\text{Ni/Ce}_x\text{Nb}_{1-x}\text{O}_2$ samples under 5% H_2/He mixture.

concentrations on ceria. According to Table 5, the amount of Nb^{4+} increased as the concentration of the niobium decreased, which was also reported by You et al. [19]. For niobium containing calcined samples, the surface Ce/Nb ratios indicated that the surface is enriched with Nb, regardless of Nb content.

The Ce 3d spectra is composed by two multiplets (v and u). These multiplets correspond to the spin-orbit split of $3d_{5/2}$ and $3d_{3/2}$ core holes. The u'' is the most representative peak of Ce^{4+} state [50], while v' and u' lines indicate the presence of Ce^{3+} ions. According to the surface composition (Table 5) the presence of niobium favored the presence of Ce^{3+} . Ni/CeO_2 calcined sample has mainly Ce^{4+} on the surface, while $\text{Ni/Ce}_{0.80}\text{Nb}_{0.20}\text{O}_2$ showed a mixture of $\text{Ce}^{3+}/\text{Ce}^{4+}$ oxidation states, indicating that the surface of the sample is not fully oxidized.

After the reduction process (at 500 °C for 1 h), the Ni 2p_{3/2} core level spectra showed binding energies characteristic of Ni^+ and Ni^{2+} (B.E. = 852.2 eV and 855 eV, respectively). It was clear that none of the samples were completely reduced [51]. The absence of complete reduction in the XPS experiment may be caused by the use of diluted

hydrogen flow in this analysis. After reduction treatment, almost all the catalysts showed a strong decrease in the intensity of the Ni 2p_{3/2} core level, which corresponds to a decrease in the fraction of metallic Ni exposed on the surface [47]. This decrease may be an indicative of sintering phenomena of nickel particles during the reduction process and/or coverage of metallic particles by the support. The amount of metallic nickel surface exposed decreases in the following order: $\text{Ni/CeO}_2 > \text{Ni/Ce}_{0.30}\text{Nb}_{0.70}\text{O}_2 > \text{Ni/Ce}_{0.80}\text{Nb}_{0.20}\text{O}_2$.

The experiments showed the reduction of Ce^{4+} to Ce^{3+} , which is in agreement with the XANES analysis after the pre-treatment at 500 °C for 1 h in diluted H_2 . According to the intensity of the peak u'', the fraction of Ce^{3+} species decreased in the following order: $\text{Ni/Ce}_{0.30}\text{Nb}_{0.70}\text{O}_2 > \text{Ni/Ce}_{0.80}\text{Nb}_{0.20}\text{O}_2 > \text{Ni/CeO}_2$. For $\text{Ni/Ce}_{0.30}\text{Nb}_{0.70}\text{O}_2$, only Ce^{3+} was observed on the surface. The presence of Nb promoted the formation of defect sites on the catalysts surface. In fact, $\text{Ce}^{3+}/(\text{Ce}_{\text{total}})$ ratio increased as Nb content was raised.

At the Nb 3d region, two peaks with binding energy around 209.3 and 207.3 eV were identified for $\text{Ni/Ce}_{0.30}\text{Nb}_{0.70}\text{O}_2$ and $\text{Ni/Ce}_{0.80}\text{Nb}_{0.20}\text{O}_2$,

Table 4
EXAFS parameters of Ni–Ni interactions for the studied catalysts and Ni foil reduced at 500 °C.

Sample	C.N. (Ni–Ni)	R (Å) (Ni–Ni)	e_0 (eV)	σ^2 (Å ²)	r-factor
Ni ^{foil}	12	2.4829 (0.0015)	6.43(0.66)	0.00600 (0.0004)	0.0084
Ni/CeO ₂	11.79 (0.75)	2.4825 (0.0017)	6.45(0.71)	0.00658 (0.0005)	0.0088
Ni/Ce _{0.80} Nb _{0.20} O ₂	12.08 (0.78)	2.4819 (0.0018)	6.21(0.72)	0.00639 (0.0005)	0.0090
Ni/Ce _{0.30} Nb _{0.70} O ₂	11.72 (0.74)	2.4829 (0.0017)	6.37(0.71)	0.00646 (0.0005)	0.0089
Ni/Nb ₂ O ₅	11.79 (0.75)	2.4827 (0.0017)	6.49(0.69)	0.0066 (0.0005)	0.0083

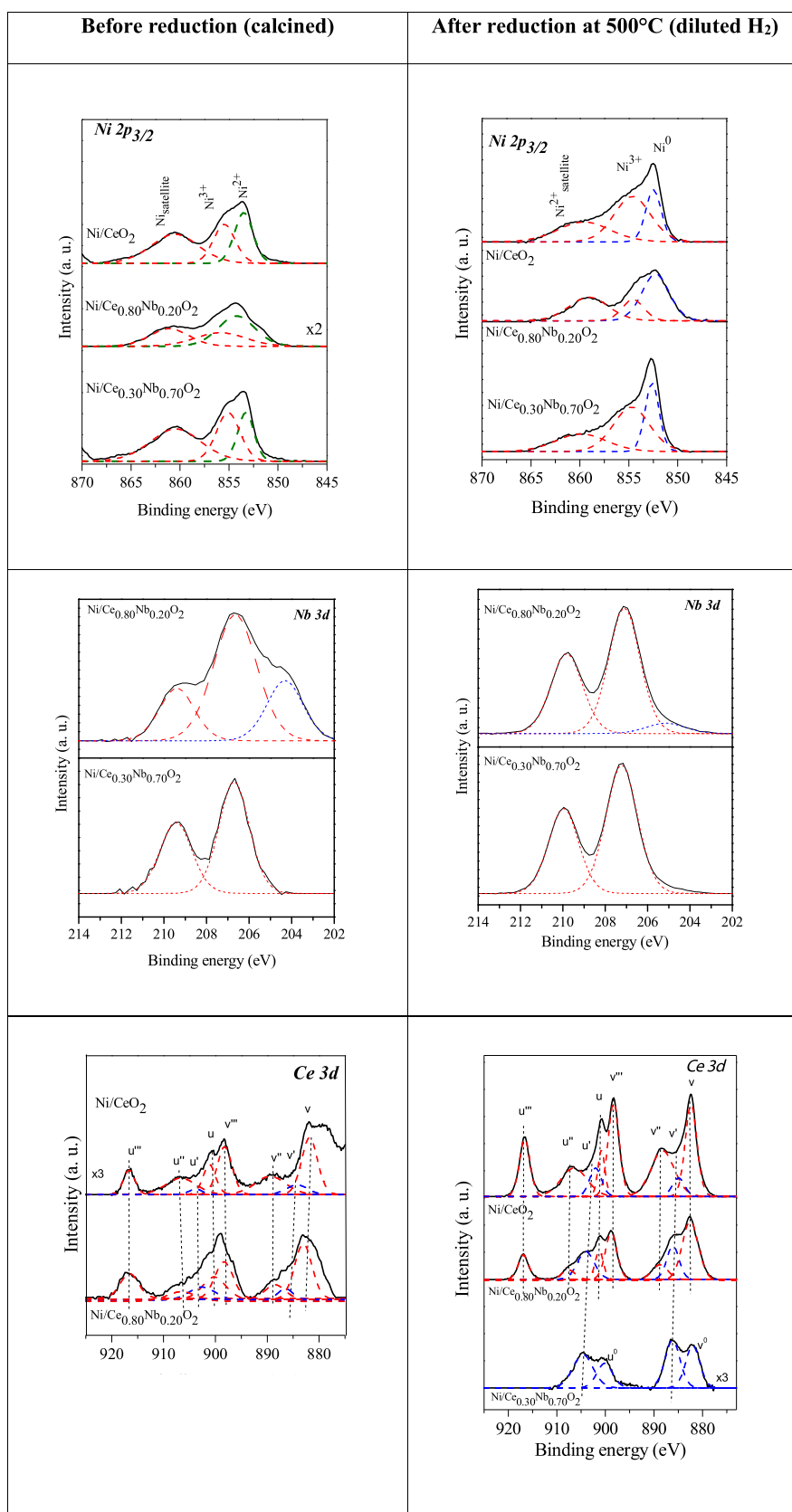


Fig. 8. XP spectra of the Ni-supported catalysts before and after reduction in diluted H₂ at 500 °C.

which corresponds to Nb⁵⁺ species. The lack in the niobium reduction observed may be related to operational conditions, as observed for the nickel spectra. The surface compositions calculations (Table 5) indicated that the pretreatment under H₂ atmosphere increased the niobium

concentration on the surface for Ni/Ce_{0.30}Nb_{0.70}O₂, which may be related to the presence of SMSI effect [54].

In summary, the characterization showed deep alterations in the structure of the studied catalysts. The addition of a small amount of Nb

Table 5
Surface composition (at %) derived from XPS analyses.

Surface Composition	Calced				Ratios			
	Ni	Ce	Nb	O	Ce ³⁺ /Ce _T	Nb/ Ce + Nb + Ni	Nb ⁴⁺ / (Nb ⁴⁺ + Nb ⁵⁺)	Ce ³⁺ /Ni ²⁺
Ni/CeO ₂	36.43	8.58	–	63.57	0.07	–	–	0.08
Ni/Ce _{0.80} Nb _{0.20} O ₂	7.17	7.61	29.34	55.87	0.14	0.66	0.26	0.36
Ni/Ce _{0.30} Nb _{0.70} O ₂	29.64	0	8.57	61.79	–	0.22	0	–

Surface Composition	After reduction				Ratios			
	Ni	Ce	Nb	O	Ce ³⁺ /(Ce _T)	Nb/Ce + Nb + Ni	Nb ⁴⁺ / (Nb ⁴⁺ + Nb ⁵⁺)	Ni/support
Ni/CeO ₂	9.5	34.2	–	55.3	0.11	–	–	0.27
Ni/Ce _{0.80} Nb _{0.20} O ₂	5.1	14.45	21.22	59.2	0.27	0.52	0.02	0.05
Ni/Ce _{0.30} Nb _{0.70} O ₂	6.3	3.3	44.2	46.3	1.00	0.8	–	0.13

favored the formation of a cubic (fcc) heterogeneous solid solution, which was indicated by the XRD and Raman analysis. As the concentration of Nb increased it was observed a prevalence of the different crystal structures, related to the Nb₂O₅ structure. The presence of Nb promoted the reduction of superficial and bulk Ce⁺⁴ to Ce⁺³, which was clearly shown by XPS and in situ XANES analyses. Although the supports showed different characteristics, EXAFS and XRD analysis indicated that the nickel average crystallite sizes were similar. In general, all the changes in structure and reducibility may have a strong influence in the activity and selectivity of these samples in the HDO reaction, which will be presented in the sequence.

3.2. HDO of phenol over Ni/Ce_xNb_{1-x}O₂ catalysts

The phenol conversion and product yield for HDO of phenol at 300 °C over all catalysts as a function of W/F are shown in Fig. 9.

The reaction rate for HDO of phenol and the selectivity to products at low phenol conversion (around 13%) are presented in Table 6. Ni/CeO₂ showed the lowest reaction rate (0.199 mmol (min.g_{cat})⁻¹), while all the niobium containing catalysts exhibited higher reaction rates. The estimation by interpolation calculations considering just the effect of the niobium concentration showed that the rate observed for Ni/Ce_{0.80}Nb_{0.20}O₂ is around 4 times higher than the expected if one considers just the support composition. This is an indication that the presence of a heterogeneous solid solution increased the activity of the catalyst. This improvement may be associated with the presence of a higher number of oxygen vacancies in the cubic (fcc) structure of the Ce_{0.80}Nb_{0.20}O₂, as observed by the lattice expansion shown through XRD analysis. Also, in situ TPR-XANES and Raman results show that the addition of Nb facilitated the reduction of ceria. According to Xiao et al. [61], there are two ways that deoxygenation reactions can occur on reducible oxides: (i) a Langmuir-Hinshelwood type mechanism happens when both H₂ and the oxygenated molecule adsorb on the surface, react and desorb as water and the deoxygenated product and (ii) a reverse Mars-Van Krevelen occurs when the vacancies of the reducible support act as a reducing site to subtract the oxygen from the oxygenated compound. Therefore, the addition of Nb would help to improve the activity.

For Ni/CeO₂ catalyst a low selectivity to benzene was observed and methane was the dominant product for W/F > 0.4 h. Significant amounts of cyclohexanone (ONE) and cyclohexanol (OL) were also formed. The addition of Nb to ceria significantly increased the selectivity to benzene and reduced the formation of methane, cyclohexanol and cyclohexanone. The presence of 20% of Nb changed

significantly the product distribution. Further increase in the Nb content continued favoring the formation of benzene, while the production of methane and oxygenated compounds was inhibited. For Ni/Ce_{0.30}Nb_{0.70}O₂ and Ni/Nb₂O₅ catalysts, only benzene was formed in the whole range of W/F studied. The positive effect of using niobia as a support was previous reported by Teles et al. [62]. According to the authors Pd/Nb₂O₅ was more active than Pd/SiO₂ catalyst for HDO of phenol. Regarding the products, benzene was the main compound formed over niobia supported catalyst, whereas hydrogenated products (cyclohexanone and methylcyclohexanone) were mainly produced on Pd/SiO₂.

3.3. The effects of supports on the reaction pathway

Two different characteristics were evaluated in the samples: structural and Nb and Ce composition. It is expected that these characteristics may affect the reaction mechanism; however, the role of each effect is not totally clear. The mechanism of HDO of phenol has been extensively studied in the literature. In general, three reaction paths were mainly reported for HDO process: (i) hydrogenation of the C_{Arom}-C (HYD) bond (ii) direct deoxygenation (DDO) and (iii) tautomerization - hydrogenation-dehydration [6–8,12,62–66]. Based on these studies, the following reaction pathways could be proposed for HDO of phenol over Ni supported on Ce_xNb_{1-x}O₂ catalysts (Scheme 1).

The catalytic results showed that product distribution are influenced by the composition of the support. For Ni/CeO₂, the high formation of cyclohexanone and methane indicates that the tautomerization of phenol followed by hydrogenation to cyclohexanone as well as the direct deoxygenation via the formation of an unsaturated hydrocarbon species followed by hydrogenolysis to C₁–C₆ hydrocarbons occur.

The addition of niobium to ceria significantly changed product distribution. Increasing the niobium content increased the selectivity to deoxygenated product (benzene), whereas the selectivity to hydrogenated (cyclohexanone and cyclohexanol) and hydrogenolysis (methane) products strongly decreased. For instance, the selectivity to benzene increased 5-fold from Ni/CeO₂ to Ni/Ce_{0.80}Nb_{0.20}O₂ and 10-fold to Ni/Ce_{0.30}Nb_{0.70}O₂. These changes cannot be justified only by the variation of bulk or surface composition of the supports. Regarding methane selectivity, it was lower for Ni/Ce_{0.80}Nb_{0.20}O₂ when comparing with Ni/CeO₂ and it was no longer detected on Ni/Ce_{0.30}Nb_{0.70}O₂ catalyst. The highest selectivity to deoxygenated products is likely due to the higher oxophilicity of Nb⁴⁺/Nb⁵⁺ cations in comparison to Ce⁴⁺/Ce³⁺ species. However, the disappearance of methane formation needs a more detailed discussion. The direct

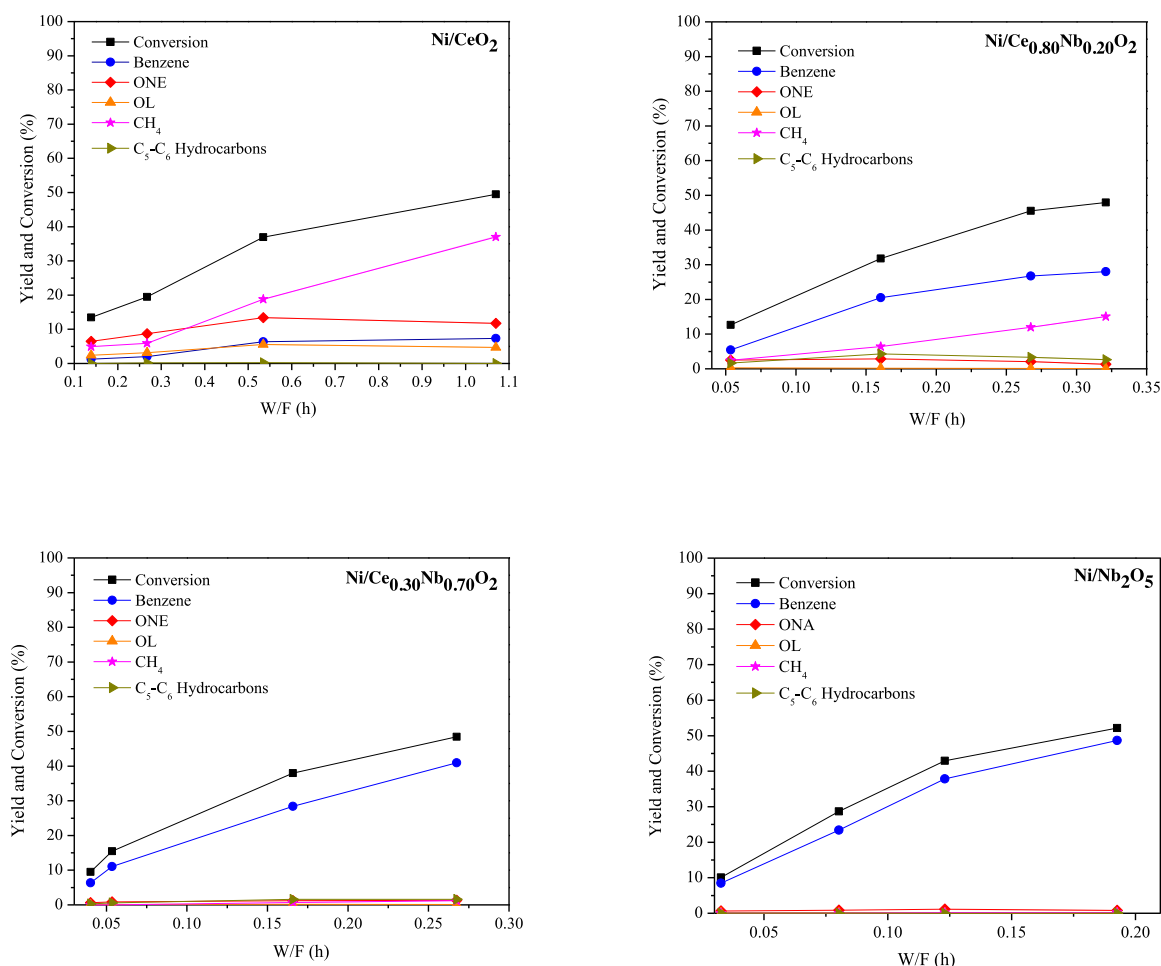


Fig. 9. Phenol conversion and yield of products as a function of W/F over the studied samples. Reaction conditions: T = 300 °C; P = 1 atm; and H₂/phenol molar ratio = 60.

hydroxylation of phenol followed by hydrogenolysis occurs mainly over more oxophilic metals such as Ru, Co and Ni. DFT calculations demonstrated that the stronger interaction of the oxygen with the oxophilic metal reduces the energy barrier necessary for the direct cleavage of the C–O bond [64]. In this case, the direct dehydroxylation produces partially unsaturated hydrocarbon species followed by hydrogenolysis to C₁–C₆ hydrocarbon. Therefore, since we used Ni-based samples, it would be expected that methane would be produced in all the catalysts. However, it is known that the support plays a key role on the reaction mechanism for HDO of phenol. More oxophilic supports such as ZrO₂, TiO₂ and Nb₂O₅ promote the hydrogenation of the carbonyl group of the keto-tautomer intermediate formed, favoring the formation of deoxygenated products [6,8,12]. The stronger interaction between the oxygen of the phenolic compound and the oxophilic site represented by Zr⁴⁺/Zr³⁺, Ti⁴⁺/Ti³⁺ and Nb⁴⁺/Nb⁵⁺ cations decreases the energy required for the cleavage of the C–O bond, favoring

the deoxygenation. Through XANES and XPS results the authors showed evidence that there is no correlation between the selectivity for deoxygenation products and the fraction of Nb⁴⁺ present in the sample.

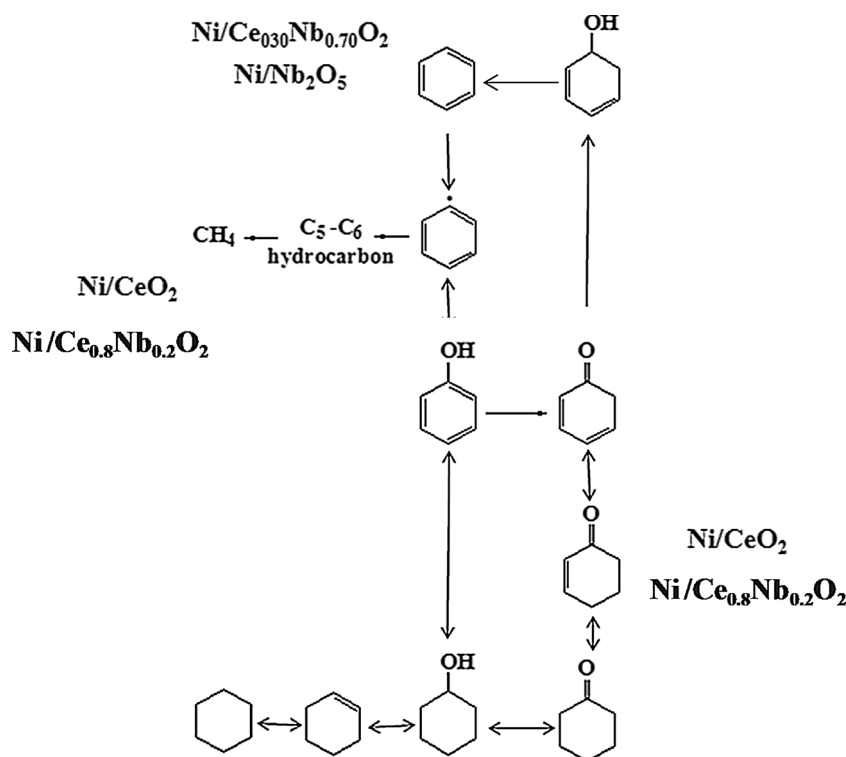
XRD analysis revealed that the samples have different crystal structures, which probably interfered in the catalytic activity. Ni/CeO₂ and Ni/Ce_{0.80}Nb_{0.20}O₂ presented Cubic (fcc) structure, since the rich cerium supports preserved the cubic (fcc) structure characteristic of ceria. Structural defects observed for Ni/Ce_{0.80}Nb_{0.20}O₂, which may be related to the presence of some Nb atoms in the ceria structure, as observed by the XRD and Raman analysis, promoted a better activity of this structure. However, for Ni/Ce_{0.30}Nb_{0.70}O₂ and Ni/Nb₂O₅ it was observed hexagonal and orthorhombic crystal structures, which probably favored the access of the phenol molecule to the structure. Recently, Macedo et al. [66] attributed the difference in catalytic performance between α-MoCl₃/CNF and β-Mo₂C/CNF to differences in the catalyst's crystal structure, more specifically, the associated site densities.

Table 6

Phenol HDO reaction rates and selectivity. Reaction conditions: T = 300 °C; P = 1 atm; H₂/phenol molar ratio = 60; phenol mass flow (L/h) = 2.91179E-06.

Samples	W/F (h)	Reaction rate (mmol (min.g _{CAT}) ⁻¹)	X [*] (%)	Selectivity (%)				
				Benzene	ANE + ENO	ONE	Methane	Cyclohexanol
Ni/CeO ₂	0.14	0.199	13.4	8.38	0	43.02	32.62	15.98
Ni/Ce _{0.80} Nb _{0.20} O ₂	0.05	0.488	12.67	44.09	13.29	20.38	19.94	2.27
Ni/Ce _{0.30} Nb _{0.70} O ₂	0.05	0.409	9.53	86.92	3.77	8.35	0	0.94
Ni/Nb ₂ O ₅	0.03	0.55	10.10	89.96	2.4	6.74	0	0.90

* Conversion.



Scheme 1. Reaction pathways for HDO of phenol over Ni supported on ceria-niobia oxides.

Overall it is important to point out that the observed changes in activity and product selectivities of Ni/CeO₂ with the addition of Nb could not be predicted based on the behavior of pure Ni/CeO₂ and Ni/Nb₂O₅ samples. Both the incorporation of Nb into the ceria's lattice and the formation of heterogeneous solid solutions, as well as the SMSI effect, had important effects on the observed results.

3.4. Stability analysis

Phenol conversion and product distributions as a function of TOS (24 h) for all catalysts are shown in [Fig. 10](#). All samples showed similar initial conversion (around 60–65%) and deactivated mainly during the first 6 h of TOS. The stability of the catalysts defined by Eq. (3.3) was calculated and the results are listed in [Table 7](#) (deactivation parameter – DP). The carbon balances are presented in Table S2. In general, the deactivation degree increased with Nb content.

The presence of cerium in the supports did not significantly improved the catalyst stability for Ni impregnated samples. De Souza et al. [6] reported that Pd supported on CeO₂ and CeZrO₂ were more stable for the HDO reaction than Pd/ZrO₂ and Pd/TiO₂ catalysts. According to the authors, phenoxy and intermediate species remains adsorbed on the Lewis acid sites, blocking those sites and inhibiting further reactant adsorption. The authors correlated the lower degree of deactivation of Pd/CeO₂ and Pd/CeZrO₂ catalysts to the higher density of oxygen vacancies of these supports. The formation of oxygen vacancies exposes additional cationic sites that turn over oxygenated intermediates and/or allow facile desorption of oxygenated products. They also suggested that the adsorption strength of the phenoxy species on the metal cation contributed to catalyst deactivation. The stronger adsorption between the carbonyl function with oxophilic sites such as Zr⁴⁺/Zr³⁺ and Ti⁴⁺/Ti³⁺ cations resulted in an accumulation of O-containing byproducts and led to catalyst deactivation.

In our work, the ceria based sample was the most stable. The increase of Nb content led to an increase in the fraction of Ce^{3+} species, as revealed by XPS and XANES. However, the higher formation of defective sites did not contribute for catalyst stability since all catalysts exhibit approximately the same deactivation degree.

There were also changes in the product distribution along the reaction time on stream (Fig. 10). For all samples, the selectivity to ONE increased, while the benzene formation decreased during 24 h of TOS. For Ni/Ce_{0.30}Nb_{0.70}O₂ and Ni/Nb₂O₅ catalysts, the only products observed at the beginning of reaction were benzene and a small amount of ONE. A possible explanation to the changes in selectivity observed for these samples is that the presence of Nb coupled to the reduction temperature of 500 °C promoted the SMSI effect over the metallic phase. The hydrogenolysis reaction proceeds by cleaving C–C bonds to form C_xH_y and CH_x species. In general, the hydrogenolysis of alkanes has been considered a structure sensitive reaction and a decrease in activity with decreasing particle size has been observed [65]. The in situ XRD and EXAFS analyses revealed that large Ni particles were formed for all catalysts, regardless of the support composition. Therefore, it should be expected that all catalysts show high selectivity to hydrogenolysis products. However, the formation of methane decreased when the Nb content increased. In this study XPS data revealed a decrease in the fraction of metallic Ni exposed on the surface after reduction at 500 °C. This could be due to the sintering of Ni particles and/or coverage of metallic particles by the support. Considering that XRD and EXAFS showed that all catalysts contain large particles, the changes in selectivity to hydrogenolysis products were not caused by the differences in Ni particle size. For instance, Ni/CeO₂ to Ni/Ce_{0.30}Nb_{0.70}O₂, have the same Ni average crystallite size but the selectivity to methane is completely different. Then, the differences in product distribution are also caused by the enrichment of the surface with niobium during reduction at 500 °C. These results suggest that partially reduced NbO_x species formed migrated to the surface of Ni particles. This corresponds to the so-called strong metal support interaction (SMSI) effect that has been extensively studied in the past [40,41,67–69]. The diluting effect of NbO_x patches on the surface of Ni particles (ensemble effect) should affect more significantly the structure sensitive reactions such as hydrocarbon hydrogenolysis [67–69]. The SMSI effect could be responsible for the strong decrease in the selectivity to methane observed on the Nb-rich catalysts. However, the selectivity to CH₄ increased after 24 h of TOS, which may be related to the removal of NbO_x species from the surface of Ni particles caused by the presence of H₂O produced in the reaction [67–69].

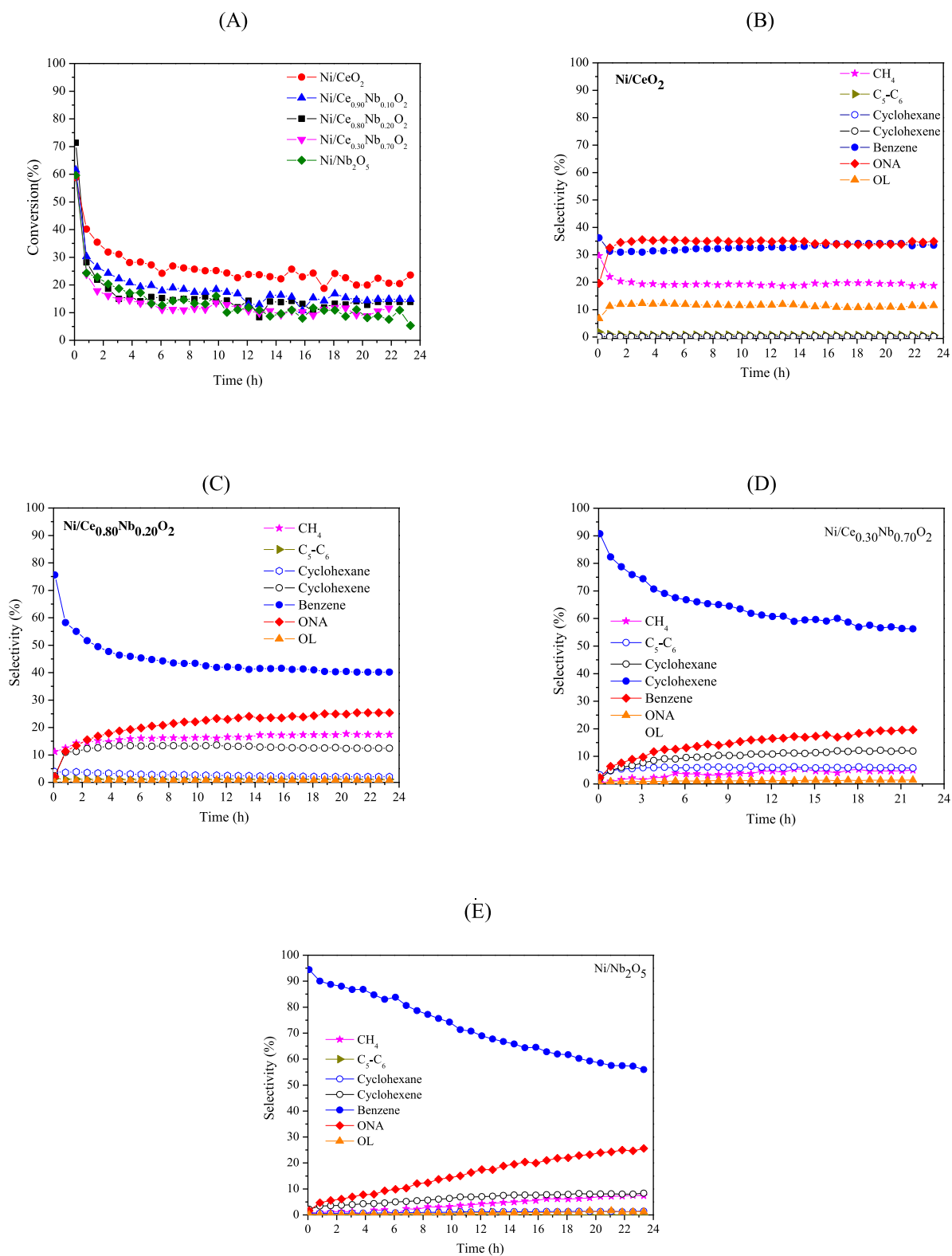


Fig. 10. Conversion of phenol (A) and selectivity to products as a function of TOS for: (B) Ni/CeO₂; (C) Ni/Ce_{0.80}Nb_{0.20}O₂; (D) Ni/Ce_{0.30}Nb_{0.70}O₂; (E) Ni/Nb₂O₅. Cyclohexanone (ONE); cyclohexanol (OL).

4. Conclusions

The objective of this work was to study samples with different Nb and Ce composition and consequently many crystal structures in order to obtain selective nickel catalysts for phenol hydrodeoxygenation reaction. The deoxygenation capacity of the samples was enhanced by the

addition of niobium, suggesting that the oxyphilic properties of the niobium are responsible to promote the deoxygenation of the studied molecule. For Ni/CeO₂ the phenol tautomerization followed by hydrogenation to cyclohexanone as well as the hydrogenolysis with the formation of methane were the main reaction pathways. XRD, Raman and TEM analyses showed different structures for the supports studied

Table 7

Deactivation parameters (DP) of the studied samples.

Samples	DP
Ni/CeO ₂	0.17
Ni/Ce _{0.80} Nb _{0.20} O ₂	0.12
Ni/Ce _{0.30} Nb _{0.70} O ₂	0.14
Ni/Nb ₂ O ₅	0.10

in this work. For Ni/Ce_{0.30}Nb_{0.70}O₂ and Ni/Nb₂O₅ the Nb₂O₅ structure prevails, while for Ni/Ce_{0.80}Nb_{0.20}O₂ and Ni/CeO₂ the manly structure was the cubic (fcc) characteristic of CeO₂. In general, Nb₂O₅ structures favored the activity of the samples. The addition of niobium increased the reducibility of cerium oxide since higher fraction of Ce³⁺ species was obtained in the doped catalyst after reduction at 500 °C in comparison to Ni/CeO₂. XPS and XANES analyses indicated a redox reaction between Ce³⁺ (defect site) and Nb⁵⁺ on the studied samples. The presence of these defective sites promoted an improvement in the reaction rate for Ni/Ce_{0.80}Nb_{0.20}O₂, while the niobium enriched surface was responsible for the increase in the benzene selectivity.

Acknowledgments

We acknowledge the financial support of National Council for Scientific and Technological Development (CNPq), Coordination of Improvement of Higher Level Personnel (CAPES) and Foundation for Research Support of the State of Minas Gerais (FAPEMIG). We would like to thank you the Companhia Brasileira de Metalurgia e Mineração (CBMM) for providing the niobium oxalate. We also thank Brazilian National Synchrotron Light Laboratory (LNLS) for the use of XDS, XPD, XAFS2 and DXAS beamlines and XPS and TEM equipment.

Appendix A. Supplementary data

Supplementary material related to this article can be found, in the online version, at doi:<https://doi.org/10.1016/j.apcatb.2018.12.040>.

References

- W. Wang, Y. Yang, H. Luo, T. Hu, W. Liu, Catal. Commun. 12 (2011) 436–440.
- D. C. Elliott, 21, 2007, 1792–1815.
- R.N. Olcese, M. Bettahar, D.M. Petjeau, B. Malaman, F. Giovannella, A. Dufour, Applied Catal. B-Environ. 115 (2012) 63–73.
- H.Y. Zhao, D. Li, P. Bui, S.T. Oyama, Appl. Catal. A-Gen. 391 (2011) 305–310.
- A. Gutierrez, R.K. Kaila, M.L. Honkela, R. Slioor, A.O.I. Krause, Catal. Today 147 (2009) 239–246.
- P.M. de Souza, R.C. Rabelo-Neto, L.E.P. Borges, G. Jacobs, B.H. Davis, D.E. Resasco, F.B. Noronha, ACS Catal. 7 (2017) 2058–2073.
- C.A. Teles, R.C. Rabelo-Neto, J.R. de Lima, L.V. Mattos, D.E. Resasco, F.B. Noronha, Catal. Lett. 146 (2016) 1848–1857.
- A.M. Barrios, C.A. Teles, P.M. de Souza, R.C. Rabelo-Neto, G. Jacobs, B.H. Davis, L.E.P. Borges, F.B. Noronha, Cat. Today 302 (2017) 115–124.
- Y. Hong, H. Zhang, J. Sun, K.M. Ayman, A.J.R. Hensley, M. Gu, M.H. Engelhard, J. Mcewen, Y. Wang, ACS Catal. 4 (2014) 3335–3345.
- P.M. Mortensen, J.D. Grunwaldt, P.A. Jensen, K.G. Knudsen, A.D. Jensen, Appl. Catal. A-Gen. 407 (2011) 1–19.
- C.R. Lee, J.S. Yoon, Y.W. Suh, J.W. Choi, J.M. Ha, D.J. Suh, Y.K. Park, Catal. Commun. 17 (2012) 54–58.
- P.M. de Souza, R.C. Rabelo-Neto, L.E.P. Borges, G. Jacobs, B.H. Davis, U.M. Graham, D.E. Resasco, F.B. Noronha, ACS Catal. 5 (2015) 7385–7398.
- S.M. Schimming, O.D. Lamont, M. König, A.K. Rogers, A.D. D'Amico, M.M. Yung, C. Sievers, Chem. Sus. Chem. 8 (2015) 2073–2083.
- J. Mikulova, S. Rossignol, F. Gérardy, D. Mesnard, C. Kappenstein, D. Duprez, J. Solid State Chem. 179 (2006) 2511–2520.
- Z. Zhang, Y. Wang, J. Lu, M. Wang, M. Li, X. Liu, F. Wang, ACS Catal. 6 (2016) 8248–8254.
- J.L. Ayastuy, A. Iglesias-González, M.A. Gutiérrez-Ortiz, Chem. Eng. J. 244 (2014) 372–381.
- M. Kurnatowska, W. Mista, P. Mazur, L. Kepinski, Appl. Catal. B-Environ. 148 (2014) 123–135.
- Y. Liu, L. Luo, Y. Gao, W. Huang, Appl. Catal. B-Environ. 197 (2016) 214–221.
- R. You, X. Zhang, L. Luo, Y. Pan, H. Pan, J. Yang, L. Wu, X. Zheng, Y. Jin, W. Huang, J. Catal. 348 (2017) 189–199.
- N. Li, G.W. Huber, J. Catal. 270 (2010) 48–59.
- C.E. Hori, H. Permana, K.Y. Ng Simon, A. Brenner, K. More, K.M. Rahmoeller, D. Belton, Appl. Catal. B-Environ. 16 (1998) 105–117.
- D. Stošić, S. Bennici, V. Rakić, A. Auroux, Catal. Today 192 (2012) 160–168.
- P. Chen, I. Chen, J. Am. Ceram. Soc. 76 (1993) 1577–1583.
- T. Negas, R.S. Roth, C.L. McDaniel, H.S. Parker, C.D. Olson, Mat. Res. Bull. 12 (1977) 1161–1171.
- J.G. Thompson, R.L. Withers, F.J. Brink, J. Solid State Chem. 143 (1999) 122–131.
- A. Chretien, D. Bodiot, C. R. Acad. Sci. II 263 (1966) 882.
- R.D. Bayliss, S.S. Pramana, T. An, F. Wei, C.L. Kloc, A.J.P. White, S.J. Skinner, T.J. White, T. Baikie, J. Solid State Chem. 204 (2013) 291–297.
- S. Danyanova, B. Pawelec, K. Arishtirova, M.V. Martinez Huerta, J.L.G. Fierro, Appl. Catal. A-Gen. 337 (2008) 86–96.
- B.M. Reddy, A.J. Khan, Y. Yamada, T. Kobayashi, S. Loridant, J. Volta, Phys. Chem. Earth Part B Hydrol. Ocean. Atmos. 107 (2003) 5162–5167.
- I.E. Wachs, J. Jehng, F. Hardcastle, Solid State Ion. 32 (1989) 904–910.
- K.J. Griffith, A.C. Forse, J.M. Griffin, C.P. Grey, J. Am. Chem. Soc. 138 (2016) 8888–8899.
- R.M. Pittman, A.T. Bell, J. Phys. Chem. 2 (1993) 12178–12185.
- G.W. Graham, W.H. Weber, C.R. Peters, R. Usman, J. Catal. 313 (1991) 310–313.
- J.R. McBride, K.C. Hass, B.D. Poindexter, W.H. Weber, J. Appl. Phys. 76 (1994) 2435–2441.
- H. Vidal, J. Kašpar, M. Pijolat, G. Colon, S. Bernal, A. Cordón, V.F. Perrichon, Appl. Catal. B-Environ. 27 (2000) 49–63.
- S. Deshpande, S. Patil, S.V. Kuchibhatla, S. Seal, Appl. Phys. Lett. 87 (133113) (2005) 1–4.
- W. Dong, H. Roh, K. Jun, S. Park, Y. Oh, Appl. Catal. A-Gen. 226 (2002) 63–72.
- P. Biswas, D. Kunzru, Int. J. Hydrogen Energ. 32 (2007) 969–980.
- C. de Leitenburg, A. Trovarelli, J. Llorca, F. Cavani, G. Bini, Appl. Catal. A-Gen. 139 (1996) 161–173.
- L.K. Frevel, H.W. Rinn, Anal. Chem. 27 (1955) 1329.
- E.I. Ko, J.G. Weissman, Catal. Today 8 (1990) 27–36.
- E. Kumar, P. Selvarajan, K. Balasubramanian, Recent Res. Sci. Technol. 2 (2010) 37–41.
- T.J.B. Holland, S.A.T. Redfern, Mineralogical Mag. 61 (1997) 65–77.
- A.A.A. da Silva, N. Bion, F. Epron, S. Baraka, F.C. Fonseca, R.C. Rabelo-Neto, L.V. Mattos, F.B. Noronha, Appl. Catal. B-Environ. 206 (2017) 626–641.
- E. Ramirez-Cabrera, N. Laosiripojana, A. Atkinson, D. Chadwick, Catal. Today 78 (2003) 433–438.
- S. Rossignol, F. Gérard, D. Mesnard, C. Kappenstein, D. Duprez, J. Mater. Chem. 13 (2003) 3017–3020.
- B. Coughlan, M.A. Keane, Zeolites 11 (1991) 1–11.
- J. Jeanjean, S. Djemel, M.F. Guilleux, D. Delafosse, Phys. Chem. 85 (1981) 4145.
- M.V. Kuznetsov, A.S. Razinkin, E.V. Shalueva, J. Struct. Chem. 50 (2009) 536–543.
- A. Froideval, C. Degueldre, C.U. Segre, M.A. Pouchon, D. Grolimund, Corros. Sci. 50 (2008) 1313–1320.
- A. Iriondo, V.L. Barrio, J.F. Cambra, P.L. Arias, M.B. Güemez, R.M. Navarro, M.C. Sánchez-Sánchez, J.L.G. Fierro, Top. Catal. 49 (2008) 46–58.
- M.R. Antonio, I. Song, H. Yamada, J. Solid State Chem. 192 (1991) 183–192.
- K. Sasaki, L. Zhang, R.R. Adzic, Phys. Chem. Chem. Phys. 10 (2008) 159–167.
- C. Cartier, T. Hammouda, M. Boyet, O. Mathon, D. Testemales, B. Moine, Am. Mineral. 100 (2015) 2152–2158.
- J. Zhang, Z. Wu, T. Liu, T. Hu, Z. Wu, X. Ju, J. Synchrotron Rad. 8 (2001) 531–532, <https://doi.org/10.1107/S0909049500016022>.
- F. Zhang, P. Wang, J. Koberstein, S. Khalid, S. Chan, Surf. Sci. 563 (2004) 74–82.
- S.H. Overbury, D.R. Huntley, D.R. Mullins, G.N. Glavie, Catal. Lett. 51 (1998) 133–138.
- Y. Li, X. Wang, C. Xie, C. Song, Appl. Catal. A-Gen. 357 (2009) 213–222.
- A.P. Grosvenor, M.C. Biesinger, R. St. C. Smart, N. S. McIntyre, Surf. Sci. 600 (2006) 1771–1779.
- S. Djemel, M. Guilleux, J. Jeanjean, J.F. Tempere, D. Delafosse, J. Chem. Soc. Faraday Trans. I 78 (1982) 835–843.
- X. Xiao, H. Bergstrom, R. Saenger, B. Johnson, R. Sun, A. Peterson, Catal. Sci. Technol. 8 (2018) 1819–1827.
- C.A. Teles, P.M. de Souza, R.C. Rabelo-Neto, M.B. Griffin, C. Mukarakate, K.A. Orton, D.E. Resasco, F.B. Noronha, Appl. Catal. B 238 (2018) 38–50.
- C.A. Teles, R.C. Rabelo-Neto, G. Jacobs, B.H. Davis, D.E. Resasco, F.B. Noronha, Chem. Cat. Chem. 9 (2017) 2850–2863.
- Q. Tan, G. Wang, L. Nie, A. Dinse, C. Buda, J. Shabaker, D.E. Resasco, ACS Catal. 11 (2015) 6271–6283.
- D.W. Flaherty, E.J. Iglesia, Am. Chem. Soc. 135 (2013) 18586–18599.
- L.S. Macedo, R.R. Oliveira, T. van Haasterecht, V.T. da Silva, H. Bitter, Appl. Catal. B 241 (2019) 81–88.
- Q.N. Xia, Q. Cuan, X.H. Liu, X.Q. Gong, G.Z. Lu, Y.Q. Wang, Angew. Chemie - Int. 53 (2014) 9755–9760.
- Y. Shao, Q. Xia, X. Liu, G. Lu, Y. Wang, Chem. Sus. Chem. 8 (2015) 1761–1767.
- X. Zhuang, Q. Xia, Y. Wang, S.C.E. Tsang, X. Gong, Int. J. Hydrogen Energ. 41 (2016) 18502–18508.